F. Maggi, S. Dossi, C. Paravan, L. Galfetti, R. Rota, S. Cianfanelli, G. Marra
Iron Oxide as Solid Propellant Catalyst: a Detailed Characterization
Acta Astronautica, Vol. 158, 2019, p. 416-424
doi:10.1016/j.actaastro.2018.07.037

Iron oxide as solid propellant catalyst: a detailed characterization

F. Maggi[a], S. Dossi[b]*, C. Paravan[c], L.Galfetti[d], R. Rota[e], S. Cianfanelli[f] and G. Marra[g]

[a] *Politecnico di Milano, Dept.of Aerospace Science and Technology, filippo.maggi@polimi.it*
[b] *Politecnico di Milano, Dept. of Aerospace Science and Technology, stefano.dossi@polimi.it*
[c] *Politecnico di Milano, Dept. of Aerospace Science and Technology, christian.paravan@polimi.it*
[d] *Politecnico di Milano, Dept. of Aerospace Science and Technology, luciano.galfetti@polimi.it*
[e] *Politecnico di Milano, Dept. of Aerospace Science and Technology, riccardo1.rota@mail.polimi.it*
[f] *AVIO S.p.A., Dept. Laboratories & NDT, Colleferro, Italy, stefano.cianfanelli@avio.com*
[g] *Eni Donegani Research Center for Renewable Energies and Environment, Dept of Chemical Physics (CHIFIS), Novara, Italy, gianluigi.marra@eni.com*
* Corresponding Author

Abstract

Hematite represents the most common burning rate modifier used in propellant production. The tuning of burning rate is obtained even for amounts ranging below 1 wt.% of the total composition. Different studies have evidenced a role in ammonium perchlorate dissociation while there are not enough literature documents to clearly support or oppose its capability to enhance binder decomposition. The acceptance of such ingredient in an industrial environment is based mostly on the verification of few parameters, relevant to catalytic action (namely, particle size, specific surface area). The complexity of the iron oxide family shows a wide set of features, neglected in standard quality check but important for a detailed characterization. Such properties assist in defining a unique fingerprint of the material and can be used for detailed identification of batch-to-batch reproducibility, for new supplier qualification, or for improvement of basic knowledge. The present paper is an extract of a detailed characterization activity performed on different batches of nominally identical propellant-grade hematite. Reported results show peculiar properties of the ingredients and characterization methodologies specifically employed for the scope, proposing an end-to-end batch analysis for full ingredient back-trace capability in the supply chain.

Keywords: hematite, catalysis, propellant, quality assurance, supply chain back-trace capability

Nomenclature

A	pre-exponential factor (Vieille's law)	Δm_i	mass increment associated to the i-th peak
a_s	SSA-based mean particle diameter	ΔH_i	reaction enthalpy of the i-th peak
D_{10}	number-weighted mean diameter	ρ	Density
D_{32}	surface-weighted mean diameter	$\alpha, \beta, \gamma, \varepsilon, \zeta$	crystalline phases
D_{43}	volume-weighted mean diameter		
d(x)	diameter of the x percentile		
$m_{\%}$	instantaneous normalized mass		
N	exponent (Vieille's law)		
P	pressure		
R^2	coefficient of correlation		
r_b	burning rate		
$T_{on,i}$	onset temperature of the i-th peak		
T_{end}	temperature at the end of a peak		

Acronyms/Abbreviations

AP	ammonium perchlorate	SSA	specific surface area
DSC	differential scanning calorimetry	TG	thermogravimetry
DTA	differential thermal analysis	XPS	X-ray photoelectron spectroscopy
GIXRD	grazing-incidence X-ray diffraction	XRD	X-ray diffraction
HTPB	hydroxyl-terminated polybutadiene	XRF	X-ray fluorescence
ICP	inductive coupled plasma	SEM	scanning electron microscopy

1. Introduction

Iron oxide (Fe_2O_3, hematite) in solid propellants is commonly adopted as a ballistic modifier. The role of iron oxide consists of tuning the ballistic properties of the propellant. The fraction used is almost negligible, in comparison to other ingredients (in the range of some fraction of percent to some percent) [1]. The literature is rich of inhomogeneous data about the effect of this catalyst and, as a general conclusion, its action is strongly dependent on the composition under testing (specifically, the ions included in the oxidizer) and the amount used. In propellants based on ammonium perchlorate (AP), the effect is sensible and is rated up to about 100% of burning rate increment, within the entire pressure range [2]. However, this effect is obtained when a limited hematite fraction is used, between 1 and 5 wt.% in the whole propellant composition [3]. Above such limit the burning rate decreases gradually. Several tests and experimental methods have been published by authors to understand the reasons of the catalyst action, as summarized by Chakravarty et al. [2]. The behavior of iron oxide with other oxidizers showed that, presumably, the effect is connected to the perchlorate ion forming the AP molecule. Other investigations underlined the coupled aspect of both homogeneous and heterogeneous effect. The action of a proton transfer mechanism is generally accepted. The fact is that a clear vision of the process is still lacking, even though the tests on oxides in general, and iron oxide specifically, was started more than 50 years ago.

The important role of iron oxide in tuning the propellant burning rate requires careful consideration in case of batch-to-batch acceptance monitoring or choice of supplier. Currently, four production methodologies of red iron oxide are used at industrial level (Penniman, Laux, Copperas and Ningbo, this last being an environmentally friendly derivative of Penniman). All methods supply materials of varying quality, size, shape, or possible contaminants. Hence, a detailed description of such ingredient, beyond the standard investigations performed for in-line quality assessment, confers more back-trace capability in the supply chain and in product development. In this perspective, the present paper shows an end-to-end detailed comparison of two nominally identical samples of hematite. The work ranges from standard ingredient analysis up to reactivity assessments, using relevant propellant compositions.

2. The iron oxide family

The chemical nomenclature lists 16 different types of iron-based oxides, hydroxides, or oxides-hydroxides. Most of these compounds are very common in the natural environment, deriving from weathering of magmatic rocks and their further evolution. These molecules are formed mainly by combination of *Fe* and *O* ions, where the size of the *O* ion is much larger than the one of *Fe*. For this reason, the spatial displacement of oxygen imposes the crystal structure. In these compounds iron is found in the two valence states *Fe(II)* or *Fe(III)* providing tetrahedral or octahedral linkages. In nature, the only available arrangements in the third dimension of the anions are cubic close packing (ccp) and hexagonal close packing (hcp). In several cases the organization of atoms into crystals is stable from an energetic viewpoint. This grants a high energy of crystallization, favoring in most of the cases the generation of fine particles, reaching specific surface areas larger than 100 m^2/g [4].

If we strictly limit the analysis to the "Iron Oxide", both *Fe(II)* and *Fe(III)* oxides can be found (see Table 1). The crystal phases β-Fe_2O_3, ε-Fe_2O_3, and the recently discovered ζ-Fe_2O_3 are synthesized only in laboratory under specific operating conditions and are not of peculiar interest for the present analysis. The *FeO* is unstable at room temperature unless fast cooling is performed. In this case a metastable condition is obtained, producing a cation-deficient phase. The α-Fe_2O_3 is the most stable form of iron oxide and represents a common catalyst in rocket propulsion. It is amphoteric, paramagnetic and has a typical blood-red color if finely ground. It has a hexagonal close-packing structure, even though an alternative cubic close-packed structure is also known, if mild oxidation of Fe_3O_4 is provided. Its crystal shape tends to be dependent from the environment where it grows, and it is sensitive to the presence of additives [3]. It can be produced by calcination or growth in solution, being the former the most convenient method. The γ-Fe_2O_3 represents another iron (III) oxide isomer having inverse spinel structure with cation-deficient sites. It features red-brown color and has ferromagnetic properties. It can be found in nature as a weathering product of magnetite-based minerals or it can be produced by heating other oxides, mainly in presence of organic substances. Finally, the Fe_3O_4 is an amphoteric oxide, resulting from the combination of the oxidation states Fe(II) and Fe(III), arranged in mixed octahedral/tetrahedral sites (inverse spinel). It is featured by ferromagnetic properties and high electric conductivity.

Table 1: Summary of iron oxide properties

	Molar mass, g/mol	Density (g/cm^3)	Melting temperature, °C	Structure
α-Fe_2O_3 (hematite)	159.69	5.26	1565	hexagonal close-packing (Alternative: cubic close-packed)
β-Fe_2O_3	159.69	5.11.	*	Cubic, bixbyite-like structure [5,6]
γ-Fe_2O_3 (maghemite)	159.69	4.87	**	Inverse spinel [7,8]
ε-Fe_2O_3	159.69	5.08	***.	Orthorhombic [9,10,11]
ζ-Fe_2O_3	159.69	4.99	N.Av.	Monoclinic [12]
Fe_3O_4 (magnetite)	231.54	5.18	1590	$Fe^{II}Fe_2^{III}O_4$, Inverse spinel [13]
FeO (wüstite)	71.84	5.72-5.61	1377	two interpenetrating face-centered cubic structures

*: *β-Fe_2O_3 converts into α-Fe2O3 when heated above 500 °C*
**: *γ-Fe_2O_3 converts into α-Fe2O3 when heated above 400 °C*
*** *ε-Fe_2O_3 converts into α-Fe2O3 when heated above 500-750 °C depending on preparation method*

3. The catalytic action

The main iron oxide catalysts used in industrial applications are magnetite and hematite. Both are amphoteric, so they can be used in either acid or basic catalysis, in oxidation/reduction chemical processes. It was observed that the performance of the material depends from the specific surface area. For this reason, most of these ingredients are nanometric (from few hundreds down to few nanometers). In this respect, the efficacy of the dispersion and the placement with respect to the main reactant play significant roles. Results in this direction are obtained for AP/hematite mixtures by Ma and co-authors. In their work the improvement of AP decomposition is obtained when proximity between the oxidizer and the iron compound is obtained by production of AP/Fe_2O_3 composites [14].

Within the list of the reactions involving iron oxide catalysis, we can find ammonia generation from hydrogen/nitrogen reaction, dehydrogenation of some hydrocarbons, high-temperature water/gas shift reaction ($CO+H_2$). It appears that the action is obtained when hydrogen molecules are involved and, so, proton transfers. A complete overview is reported in a review book by Cornell and Schwertmann [4].

Studies regarding the role of catalysts in the decomposition path of ammonium perchlorate are abundant in the literature, if hematite is considered. In thermogravimetric analyses of AP and iron oxide mixtures an anticipation of the decomposition reaction onset is obtained for the oxidizer. As expected, no change occurs in phase transition. Joshi and co-authors published a paper about the activity of nanometric oxide [15]. They tested different mass fractions with three sizes (30 μm, 30 nm and 3.5 nm), showing that the micrometric iron oxide does not lead to significant improvements while the anticipation of the decomposition peak is clearly visible as the finer powders are used.

Few data are available for the catalysis of other iron oxide types on ammonium perchlorate. About magnetite, the effect of particle shape and concentration has been investigated by Wang and Yao [16]. This compound demonstrates to be an effective catalyst, anticipating both the onset of the main decomposition reaction and the offset of the mass sublimation. As expected, the reactivity is dependent from both shape and size of the powders. This cross influence suggests that the dominating parameter is represented by the specific surface area of the samples. Another work by Oyumi focused on the comparison between magnetite and hematite catalytic actions. The reference energetic material was an azide propellant containing ammonium perchlorate. Tests have demonstrated that, under such operating conditions, magnetite performs better in terms of decomposition onset and offset [17]. Moreover, propellants feature a lowered pressure exponent.

The pyrolysis of the binder assisted by iron oxide is rarely addressed in the open literature. There are some mentions in papers regarding propellant studies (e.g. Chakravarthi et al. [2], Patil and co-authors [18]) but specific works are lacking. Some information can be gathered from the literature relevant to hybrid rocket motor performance analysis. Frederick and co-authors reported regression rate investigations of solid fuels made by an oxidizer-lean composition of AP and HTPB. Some of the formulations included also hematite as a catalyst. Experimental results evidenced an increment of the regression rate in presence of AP and of AP/Fe_2O_3. The catalyst effect was more marked as the oxidizer load was incremented [19]. Some information on polyurethane decomposition in presence of metal oxides can be found in the literature about fire protection [20]. In a paper by Liu and co-authors the reduction of smoke and the increment of charring on the burning surface is obtained by adding hematite. Metal cations, and iron (III) oxide specifically, are known to catalyze the generation of double bonds, supporting cross-linking during pyrolysis process and promoting the generation of porous char layer.

Finally, iron (III) oxide and aluminum are known to generate a thermite process, involving the exchange of oxygen between the oxide and the metal, with liberation of heat. A three-step reaction is identified, involving the generation of other iron oxides (Magnetite and Wustite) as intermediate products [21]. Currently, it is not clear if such reaction is present on the burning surface of a metalized propellant, even though the high energy barrier, the low oxide concentration, and the lack of direct contact between the ingredients when dispersed in a binder may prevent from achieving it.

4. Identification and analysis

The role of iron oxide during combustion is based on a solid-gas interaction and can be assimilated to a heterogeneous catalysis. Its reaction capability is dependent from the surface properties of the material, including porosity. In addition, the heterogeneous interaction at the interface may be perturbed by the electronic structure of the molecules, when the typical catalyst dimension is 10 nm or smaller. If larger, the interaction is mostly influenced by the surface properties [22].

Laser diffraction and dynamic light scattering techniques can be routinely used for the initial assessment of particle sizes, but special care is required due to dispersion issues when the typical powder dimension falls within the micrometric range. Nitrogen adsorption can characterize the properties related to the catalytic action, such as specific surface area or porosity on the basis of Brunauer-Emmett-Teller, BET, approach [23]. From the reactivity viewpoint, the application of thermal analysis supplies direct information regarding anticipation of onset temperatures. Common analysis protocols involve differential thermal analysis (DTA) or differential scanning calorimetry (DSC), coupled with simultaneous or non-simultaneous thermogravimetry (TG).

The characterization of the material inner structure can be performed by spectroscopic methods, with some limitations. The X-ray diffraction (XRD) identifies the crystalline structure of the matter. It demonstrated to be effective in the field of inorganic compounds where an ordered arrangement of atoms is present, whereas amorphous state cannot be properly identified. In the case of iron oxides, the high energy of crystallization may suggest a preferential crystalline, rather than amorphous, condition. Distinctive refraction patterns are known for all iron-derived compounds and polymorphs. The X-ray photoelectron spectroscopy (XPS) does not support the present analysis. Despite the technique has the general capability of detecting both atom concentrations and the bonds by interpreting the peak shifts, in the case of iron-based compounds this is not possible because the relevant spectroscopic patterns do not present distinctive shapes. In addition, the sensitivity of the sample to ultra-vacuum conditions may cause crystal surfaces to undergo processes of relaxation or reconstruction. The former consists of the shift of interatomic distances in the bulk and change of bond angle in the first and second layer. The latter induces the propagation of the change also in the nearest neighbors [4]. If too thin layers are analyzed, X-ray methods may not be applicable. In these cases, the IR spectroscopy is a valid alternative. Crystal morphology, degree of crystallinity, metal substitutions, and other features can be identified by the shift of the peaks in the absorption spectrum. Finally, as in several chemical and metallurgical applications, the purity of the ingredient at ppm level may be assessed using inductive coupled plasma (ICP). With the same scope, X-ray fluorescence (XRF) can identify either superficial species or bulk atomic concentrations [24].

5. Experimental characterization

The characterization of two propulsion-grade iron oxides (ID names A and B) are reported in this paper. Both the materials are hematite, the exact grade being undisclosed for industrial reasons. They have been produced using the Copperas method and come from the same supplier. Details of the experimental characterizations are given hereafter.

5.1 Scanning electron microscopy

Particles and clusters morphology is obtained though SEM pictures. The images were obtained by a JEOL JSM-7600F thermal field emission scanning electron microscope at 5 kV and several magnifications. Each powder was dispersed on a metal support provided with a conductive graphite-based bi-adhesive tape and mounted on a multi-sample holder. To improve image quality, a nano-layer of *Cr* with a Denton Vacuum DESK V sputter system was applied.

The SEM images of the presented batches are reported in Figure 1 and Figure 2. Both exhibit the presence of micron-sized clusters, composed by nano-sized particles ranging from 100 nm to 400 nm. The granules feature a smooth superficial texture but are not spherical. Elongated particles or objects like torpedoes are visible. The presence of exotic particles with internal holes or with an extremely irregular shape is also evident. The external surface is relatively regular evidencing the typical structure of a crystal. Flat planes can be seen for the smallest particles in the 50000x images, mainly in Figure 1.

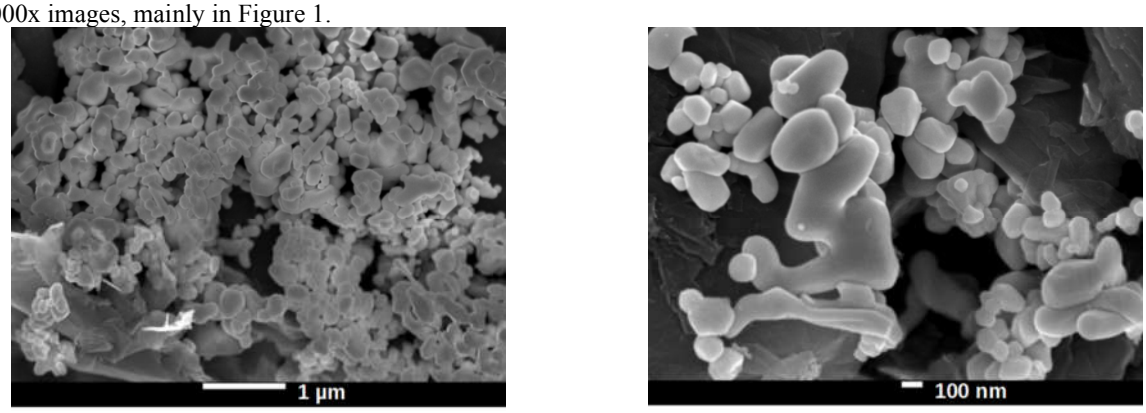

a) Magnification: 20000x b) Magnification: 50000x

Figure 1: SEM images of the sample A.

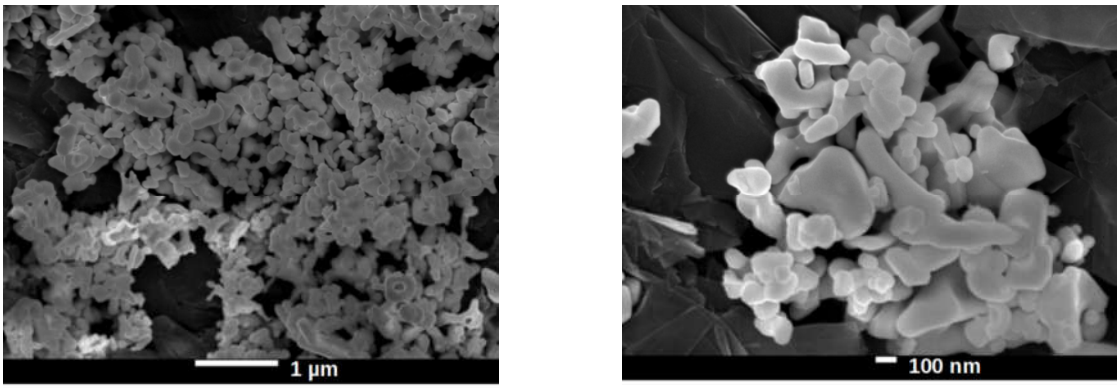

a) Magnification: 20000x b) Magnification: 50000x

Figure 2: SEM images of the sample B.

5.2X-ray diffraction

The presence of crystalline phases and the size of the domains was obtained through XRD analysis. Analyses were executed by a PANalytical X'Pert alpha-1 Θ/2Θ X-Ray Diffractometer with Bragg-Brentano geometry. The preparation consisted in positioning and leveling a small amount of powder inside a sample holder. No pretreatments were necessary being the granules sufficiently small. Tests were executed using a radiation X *Cu* Kα (λ = 1.5416 Å) at 1.6 kW. The selected angular range was 5°-90° (2Θ) with a pass of 0.02° (2Θ) and an acquisition time of 15 s/pass. The search of identified inorganic phases was performed using the Hanawal method. The crystallite size was

determined only on hematite, looking at the peak spans, using Fundamental Parameters Approach implemented in TOPAS software (Version 4.2) [25,26].

The results of the analysis are reported in Table 2. Both samples show a predominance of hematite. The batch A shows the presence of a non-negligible amount of magnetite while the lot B did not show other crystalline phases. The size of the crystallite is almost like the size of the fine fraction of the powders, meaning that mono-crystal particles may be present. It should be noted that larger crystallite size is obtained for the batch containing the magnetite impurity. It is not clear if a correlation is present between these specific parameters.

Table 2: Crystalline composition and crystallite size of the tested iron oxide batches.

Batch Sample	**Recognized Phases**		**Crystallite size, nm**
	Fe_2O_3, %	Fe_3O_4, %	
A	97.3	2.7	240
B	100.0	0.0	170

5.3 Inductive coupled plasma

The analyses were executed through a Varian 710 ICP-OES. Most intense emission line of the interested elements was selected, verifying the absence of interference with the support matrix. Sample mineralization was performed using a water/turpentine+*HF* (10%+2) solution. The suspension was then microwave-processed. All the chemicals used for the solution preparation had a maximum impurity content of 1000 ppb. Results are reported in Table 3. Among the impurities, sulfur and manganese represent the major contaminants. The former can be originated as residual of the production process. In fact, some of the synthesis methods such as the "Copperas" use sulfur-based *Fe(II)* salts as precursors and may maintain some minor contamination, despite final calcination. At authors' knowledge, unclear is the source of manganese and is probably correlated to the specific production plant. Such contaminants supply information about the quality of the powder and the relevant production process. In addition, these pieces of information are important for trace-back capability in the supply-chain of the energetic material because some influence on the combustion process cannot be excluded by the listed elements. For example, it is known from the literature a positive catalytic effect on AP decomposition of *Mn*, in form of dioxide, or an increment of the burning rate of propellants when *Mg* is added [27,28]. However, at author's knowledge there is no reported evidence of additive effectiveness at said ppm level in propellants.

Table 3: Mass fraction of impurities detected by ICP-OES technique (data in ppm)

Elements	**Batch A**	**Batch B**
Al	< 10 ± *5*	15 ± *5*
Ca	92 ± *5*	263 ± *5*
Na	108 ± *10*	320 ± *10*
Cr	34 ± *3*	12 ± *3*
Mn	954 ± *30*	1443 ± *30*
Ni	67 ± *3*	48 ± *3*
S	301 ± *20*	607 ± *20*
Si	198 ± *5*	136 ± *5*
Zn	94 ± *3*	94 ± *3*
Mg	32 ± *3*	75 ± *3*

5.4 Particle size measurement

The particle size distribution was evaluated by laser diffraction, using Malvern Mastersizer 2000 with wet dispersion (Hydro 2000S). In the data reduction approach, performed with Mastersizer 2000 software ver. 5.60, spherical and smooth-texture particles are assumed. The difference between the instrument sensor signals and the output particle size distribution is expressed in terms of percent weighted residuals. In this analysis, tests with weighted residuals larger than 5% were rejected. Two different data fitting models, supplied with the original software by Malvern, were adopted to produce the final outputs. The first one is a general-purpose model based on a broad particle size distribution (WD). The second one considers a specialized fitting that emphasizes the presence of different peaks in the powder particle size distribution (BD). A comparison between the two approaches is reported because the BD method may capture some peculiarities of the powder that are not fully caught by the WD algorithm. The iron oxide powders were dispersed in bi-distillated water. Nonidet P-40 was used as dispersant. During the analysis, the same iron oxide sample was measured multiple times. Thanks to the embedded stirring system, hydrodynamic stresses exerted by the suspending medium on the particles promoted the rupture of the (eventually present) clusters. A minimum of two reproducible tests were achieved for each lot.

Results reported in Table 4 show two sub-micrometric powders, with similar particle distribution properties. The d(0.1) settles close to range of the crystallite size. Both the mass-mean and the surface-mean diameters are sub-micrometric and the d(0.9) is slightly above one micron. Both WD and the BD model reflect similar condensed parameters.

Table 4: Particle size distribution relevant and fitting parameters; WD model.

Id.	**d(0.1) µm**	**d(0.5) µm**	**d(0.9) µm**	**D_{32}, µm**	**D_{43}, µm**
A	0.358	0.758	1.430	0.613	0.850
B	0.301	0.638	1.219	0.528	0.725

Table 5: Particle size distribution relevant and fitting parameters. BD model.

Id.	**d(0.1) µm**	**d(0.5) µm**	**d(0.9) µm**	**D_{32}, µm**	**D_{43}, µm**
A	0.416	0.559	1.456	0.628	0.801
B	0.400	0.506	1.353	0.565	0.705

5.5 Specific surface area determination

The powder SSA is determined by the BET technique based on low temperature (77 K) adsorption and desorption of N_2 [29]. The experimental setup is a Micrometrics ASAP 2000. The tested samples are pre-treated by a degas process performed for 3 hours at 300°C. The SSA data are reported in Table 6, and are completed by the indication of the volume of the surface pores. The mean particle diameter computed through the SSA information is evaluated according to Eq. (1), finding smaller size than the one found with laser diffraction and reported in Table 4 and Table 5. However, it is important to note that such values are close to the crystallite size reported in Table 2, probably indicating some residual clustering in wet dispersion or particle cohesion.

$$a_s = \frac{6}{SSA\,\rho_{\alpha\text{-}Fe2O3}} \tag{1}$$

Table 6: Specific surface area (SSA), SSA-based mean particle diameter, and pore volume of the tested iron oxide batches.

Id.	**SSA, m^2/g**	**a_s^*, nm**	**Pore Vol., cm^3/g**
A	6.3 ± 0.1	182	0.02 ± 0.01
B	7.2 ± 0.1	159	0.03 ± 0.01

6. Initial assessment of reactivity

The iron oxides have been characterized as catalysts inside propellants and slurries having composition similar to the one used in the final application. Resonant acoustic mixing was used to uniformly disperse the sample. The measurement campaigns were performed shortly after the preparation of the slurries, preventing from aging. Re-clustering attitude was not addressed. The nominal compositions are reported in Table 7. All preparations have been performed using the same batch of raw materials, except for iron oxide.

Table 7: Tested propellant compositions

Ingredient	Baseline wt.%	With hematite wt.%
Ammonium Perchlorate, AP	68.00	67.72
Micrometric aluminum	18.00	18.00
HTPB	14.00	14.00
Iron Oxide	No catalyst	0.28

6.1 Thermogravimetric tests on propellant slurries

Simultaneous thermal analyses based on DSC-TG were performed by Netzsch Jupiter 449 F5 on propellant slurries. The runs were conducted in *Ar* (mass flow rate 70 ml/min), with heating rate of 10°C/min. The investigated temperature range extended from 30°C to 1000°C. Tested samples had a mass of (3.0 ± 1.0) mg. Slurries were manufactured by resonant acoustic mixing [30] under vacuum (0.1 bar, 20-30 g acceleration) according to the quantities reported in Table 7. Reactivity data were derived from TG traces, computing temperatures of onset and end for reactions according to the tangents method [31]. The parameter $\Delta m_{\%}$ underlining the mass variation as a function of the temperature, was evaluated according to Eq. (2). For each sample two reproducible tests having difference on the onset temperatures lower than 10% were processed, reporting average and standard deviation of parameters in Table 8.

$$\Delta m_{\%} = \frac{m_{\%\text{-on}} - m_{\%\text{-end}}}{T_{\text{on}} - T_{\text{end}}} \tag{2}$$

A typical result for the baseline formulation without iron oxide, is reported in the Figure 3(a). The DSC-TG of a propellant slurry containing hematite is presented in Figure 3(b). Under the investigated conditions, additive dispersion may yield significant contributions to the data scattering between different runs. Nevertheless, the approach used in this work is consistent with other analyses reported in the open literature [18].

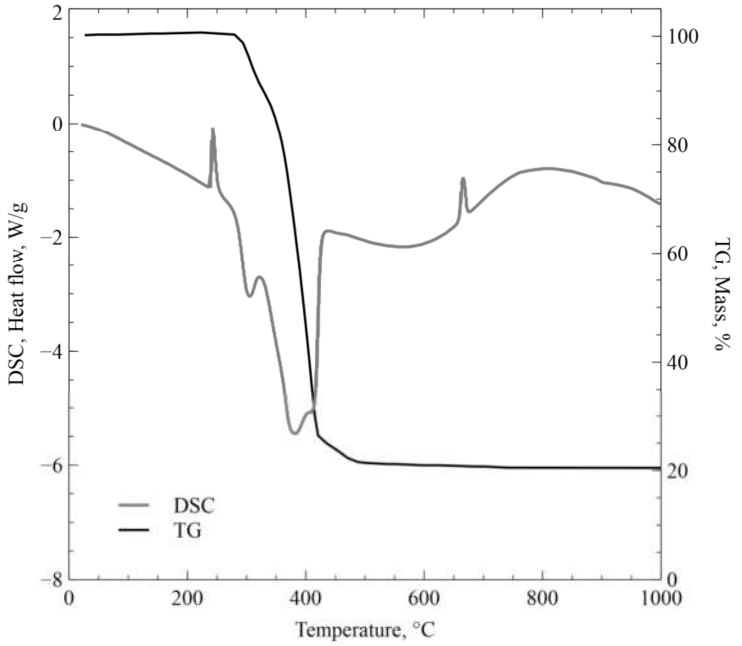

a) Baseline (no iron oxide)

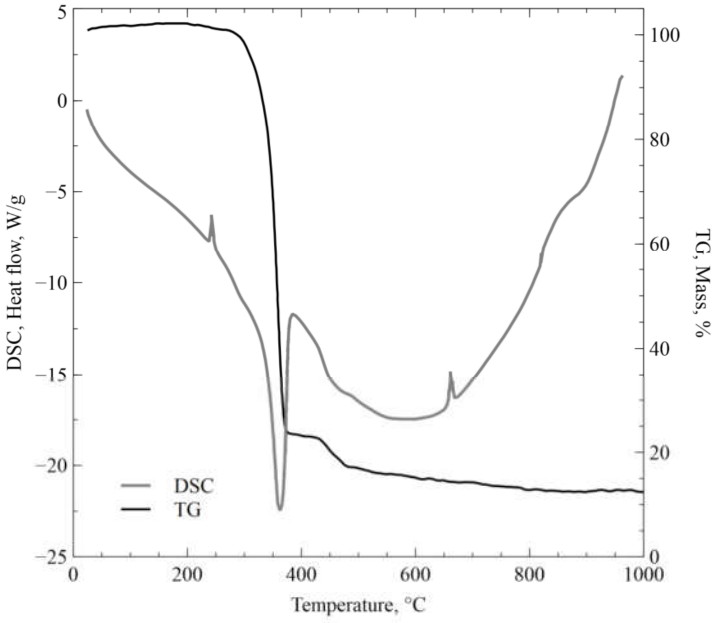

b) Sample curve with hematite (lot B)

Figure 3: Simultaneous DSC-TG run for propellant slurries. Tested condition: *Ar* (70 ml/min), 10°C/min, 30-1000°C.

Table 8: DSC-TG data for the tested propellant slurries (*Ar*, 70 ml/min, 10°C/min, 30-1000°C).

Id.	Baseline	P-A	P-B
$T_{on,1}$, °C	360.8 ± 1.5	347.4 ± 1.8	346.6 ± 1.1
Δm_1, %	-61.8 ± 6.7	-65.0 ± 5.9	-73.1 ± 1.9
ΔH_1, kJ/g	1.51 ± 0.04	2.13 ± 0.41	2.27 ± 0.01
$T_{on,2}$, °C	437.9 ± 1.8	435.3 ± 4.8	431.3 ± 0.7
Δm_{1+2}, %	-67.1 ± 7.4	-74.0 ± 5.6	-77.7 ± 2.1
ΔH_2, kJ/g	0.42 [a]	0.43 ± 0.17	0.14 ± 0.02
$\Delta m_{\%,1}$, %/°C	1.26 ± 0.03	2.73 ± 0.16	3.28 ± 0.52

[a] Single run data available

There are plenty of literature references on the thermal decomposition of ammonium perchlorate and HTPB, alone or in mix, and here only few relevant papers are reported [32,33,34,35,36]. If the reader considers the data presented in the Figure 3, the first endotherm with peak at 244°C corresponds to the orthorhombic to cubic phase transition of AP [37]. After this, an exothermic process starts (AP and HTPB decompositions). The onset of this latter reaction occurs at $T_{on,1}$ = 359.7°C and it yields a mass change Δm_1 = -66.9%. The end temperature of the reaction is $T_{end,1}$ = 419.3°C. This decomposition is followed by a second reaction with $T_{on,2}$ = 437.1°C, $T_{end,2}$ = 480.6°C, and Δm_2 = -5.7%. The enthalpy release in the two decomposition steps (as evaluated by the DSC trace) results ΔH_1 = 1.54 kJ/g, and ΔH_2 = 0.5 kJ/g respectively. The following reaction represents the Al melting with an onset at 660.8°C [38].

As expected, the iron oxide exerts no influence on the AP phase transition [18], while it lowers the onset temperature for the AP + HTPB decomposition (see $T_{on,1}$ in Table 8). The baseline propellant shows $T_{on,1}$ = (360.8 ± 1.5) °C while the formulation loaded with iron oxide from the lot A reduces the onset temperature to (347.4 ± 1.8) °C. No marked difference can be noted when comparing the two iron oxide lots. The addition of the catalyst promotes an increase in both the propellant decomposition (Δm_1) and its enthalpy release (ΔH_1). The difference between the scattering of the batches does not have peculiar significance and is justified by the dispersion of the catalyst inside a heterogeneous material with coarse particles and the typical size of the sample used for a DSC/TG run. The ΔH_1 trend is like the one exerted by Δm_1. Also in this case, the attitude of the reactivity parameter changes between the baseline and the composition containing iron oxide, having a reduced data scattering for the slurry containing the Lot B. The overall mass change (Δm_{1+2}), reported in the Table 8 does not show marked differences between the samples, being the error intervals partially overlapped.

6.2 Propellant burning rate characterization

The experimental ballistic characterization was performed in a stainless steel horizontal strand burner of 2-liter volume equipped with 2 optical accesses for propellant combustion video recording. Combustion tests were executed at different pressures in nitrogen atmosphere to avoid propellant-environment interactions. The pressure was kept constant by a set of electrovalves controlled through an analog regulator and an external gauge. Hot wire ignition was selected. The propellant was cut in samples of 4x4x30 mm, side-inhibited by a solution of low molecular weight polymer to guarantee a flat flame front. A video camera linked to a personal computer recorded the propellant combustion. A scheme of the experimental rig is reported in Figure 4. For each interested pressure, at least 3 valid videos were recorded and post processed by a proprietary software (HYDRA), capable of computing the average steady burning rate of the strand (avoiding ignition and extinction transient effects). Finally, data were correlated through a standard Vieille law $r_b = ap^n$.

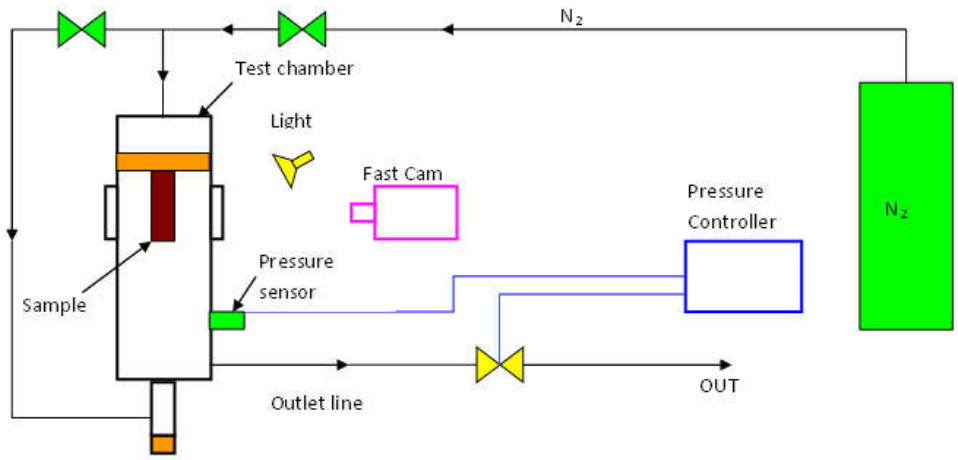

Figure 4: Scheme of the experimental rig for combustion tests

Table 9: Vieille's law of the tested propellants. Estimator of standard uncertainty is reported for coefficients. Pre-exponential factor units are (mm/s)/bar^n. Pressure is in bar.

Propellant Label	Vieilles's law	R^2
P-A	$1.57\pm0.13p^{0.42\pm0.02}$	0.982
P-B	$1.36\pm0.16p^{0.46\pm0.03}$	0.971
P-Baseline	$1.20\pm0.04p^{0.43\pm0.09}$	0.993

The result summary of the ballistic characterizations is reported in Table 9 while the plots of data fitting and burning rates at different pressures are given in Figure 5. The comparison with the baseline confirms that 0.28 wt.% of burning rate catalyst causes a sensible increment of the burning rate between 20 and 30%, without significantly affect the pressure exponent. The r_b comparison between the iron oxide lots confirms that, from a statistical point of view, there are no appreciable differences in the monitored pressure range. About the pressure sensitivity, the propellant P-A is characterized by the lowest value (n = 0.42), the propellant P-B features the highest one (n = 0.46 - 0.47). The ballistic parameter n for the baseline falls in the middle, overlapping its error bars with the ones of the other samples. Even in the pressure-by-pressure analysis of the burning rate, data from P-A and P-B are statistically indistinguishable.

1

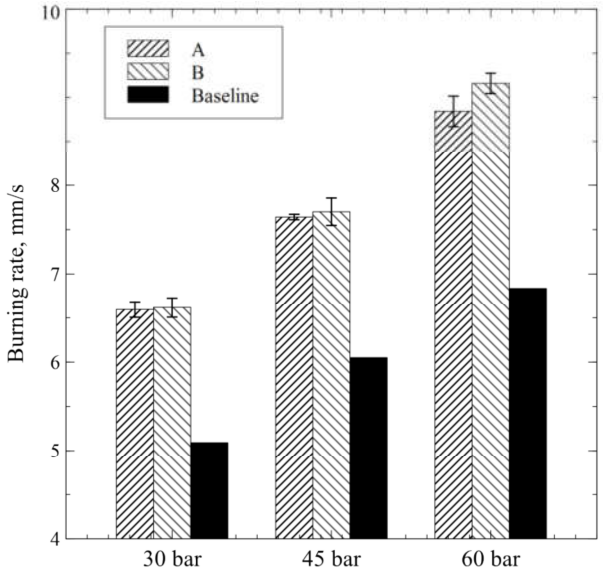

a) Pressure-by-pressure. Bars report the estimation of the statistical uncertainty.

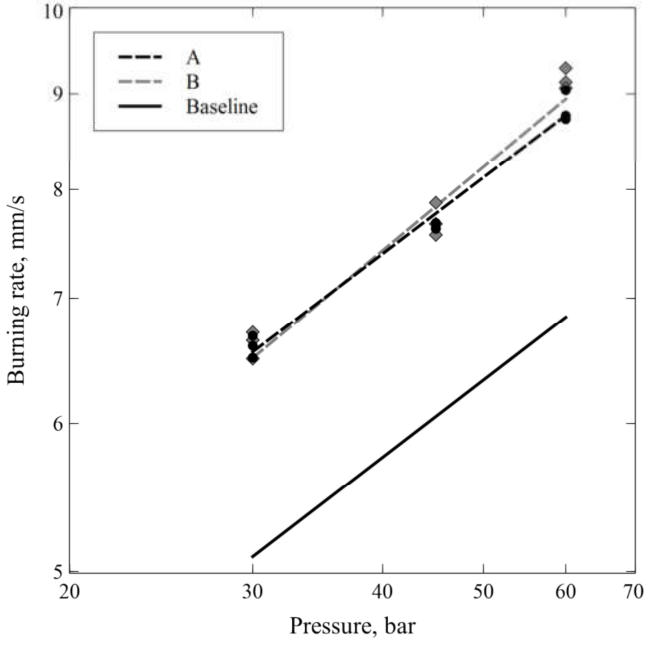

b) Power fitting

2

3 Figure 5: Burning rate of propellants containing iron oxide. Baseline data are interpolated.

4

6.3 • *Propellant extinguished surfaces*

This novel characterization consisted of the extinguishment of a propellant sample under burning conditions by depressurization below its deflagration limit and the analysis of the extinguished surface by using XRD techniques. The scope of the analysis consisted of the identification of the combustion intermediates residing on the burning surface. Sample extinguishment was performed by pressure deflagration limit in a vertical combustion chamber with optical accesses. The volume of the chamber was about 40 liters filled with rarefied nitrogen. Vacuum pump was used to evacuate the chamber and to produce low pressure. After ignition, the internal pressure was slowly decremented to ensure a quasi-steady combustion process, till the flame naturally extinguished. Extinguishment pressure was not monitored. A scheme for the chamber assembly is reported in Figure 6.

Once the propellant was extinguished, the sample was analyzed using XRD. X-ray powder diffraction data were collected at room temperature with an X'Pert PRO θ-2θ powder diffractometer with parafocusing Bragg-Brentano geometry using CuKα radiation (λ = 1.5418 Å, U = 40 kV, I = 40 mA). Data were scanned with a scintillator detector equipped with a secondary curved monochromator) over the angular range 5-90° (2θ) with a step size of 0.02° (2θ) and a counting time of 15 s/step. Inorganic phases were identified with the search method Hanawalt on PDF-2 data set (Powder Diffraction File, ICDD). Data evaluation and quantitative analysis was performed by using Rietveld method implemented in the software package Topas plus [26].

With the aim to avoid intense signal from the substrate and get stronger signal from the first 100-200 nm from the sample surface, the best way is to perform a 2θ scan with a fixed grazing angle of incidence ω, generally chosen to be slightly above the critical angle for total reflection of the sample material. This technique is popular known as GIXRD (Grazing Incident X-ray Diffraction). The GIXRD data collection parameters analysis (angular range, step size and counting time) are the same as the previous one with parafocusing Bragg-Brentano geometry, the fixed grazing angle of incidence ω is 1.0°. Examples of XRD patterns for both analytical configurations are reported in Figure 7 and Figure 8 for powder A. The quantitative analysis is reported in Table 10 and Table 11.

Samples with different cross-section area were supplied (from 4x4 mm^2 to 10x10 mm^2). In all the tests, the technique was not able to identify any iron oxide content, due to its low concentration (0.28 wt.%). The elements observed by the XRD method in Bragg-Brentano configuration consisted of the original constituents of the propellant (ammonium perchlorate and aluminum), representing the bulk of the material. For this measurement, an imprecise data uncertainty was expected because the flatness of the extinguished region is scarce. In this last case, ammonium chloride, alpha phase, is identified as AP intermediate of reaction. The reader should note that NH_4Cl does not appear in most of the kinetic schemes of ammonium perchlorate decomposition documented in the literature [39]. However, a review by Keenan and Siegmund reports a sublimation study in excess of gaseous NH_3 regarding the production of chloride ion by the reaction of ammonia and chlorine, as reported in Eq. (3). It was further demonstrated that the specific reaction was due to the suppression of perchloric acid evaporation by ammonia [40]. The reason why such reaction is taking place in the examined samples is not clear, but it may be connected to the peculiar conditions that are generated during extinction by pressure deflagration limit and, namely, low environmental pressure, rarefied nitrogen, and low propellant surface temperature.

$$8\,NH_3 + 3\,Cl_2 \leftrightarrow 6\,NH_4Cl + N_2 \tag{3}$$

The quantitative analysis of the surface composition also shows a consistent amount of metallic aluminum which exceeds the fraction of the metal in the formulation bulk. According to the Table 7, the AP/Al ratio is 79/21 by mass and 84/16 by volume but these two ingredients present different volatilization temperatures. The aluminum tends to accumulate on the burning surface, before leaving it in the shape of an agglomerate [41]. This process is more evident when approaching the pressure deflagration limit. In this peculiar burning condition the flame stretches and the temperature gradient which sustains the heat feedback towards the gas-solid interface is progressively reduced. Surface temperature and burning rate decrement till reaching oscillatory behavior and final extinction [42].

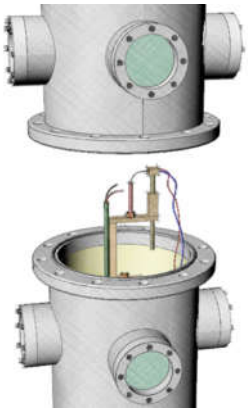

Figure 6: Scheme of the sub-atmospheric combustion chamber

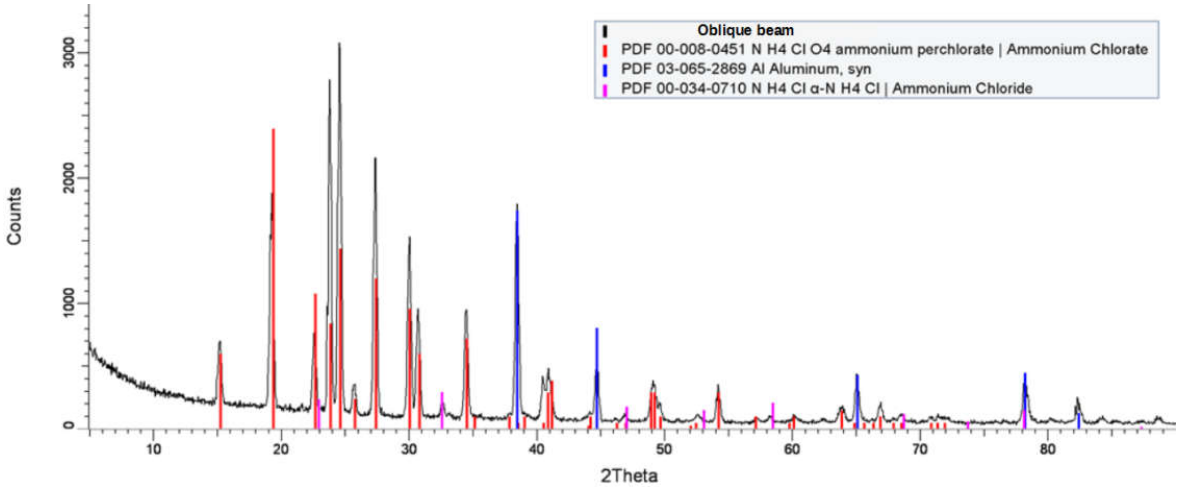

Figure 7: GIXRD analysis of extinguished surface of sample A. .

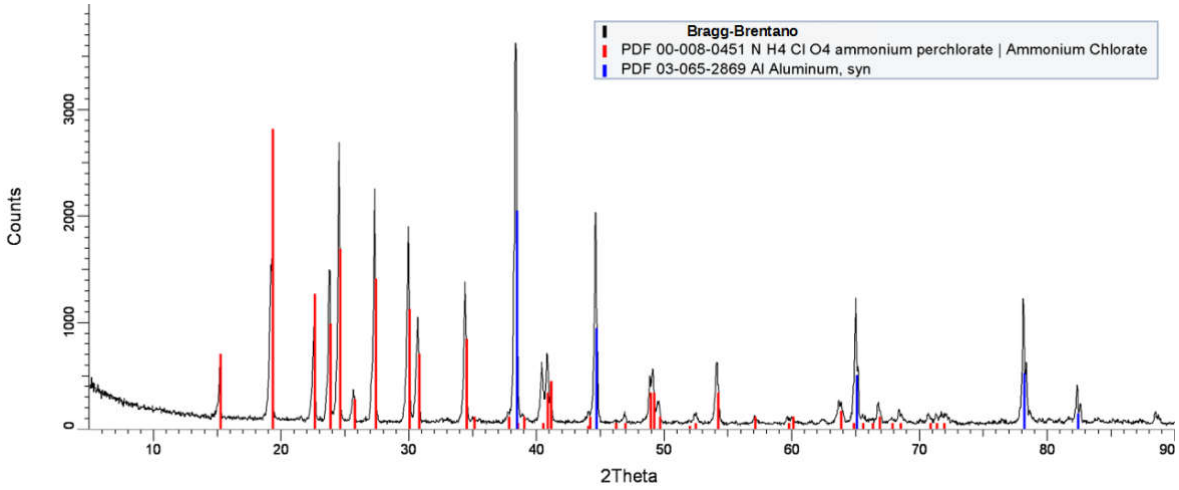

Figure 8: XRD analysis of extinguished surface of sample A. Bragg-Brentano.

Table 10: quantitative analysis of sample A extinguished surface

Id.	Grazing incidence		Bragg-Brentano	
	Mass %	Volume %	Mass %	Volume %
NH_4ClO_4	72	77	66	73
α-NH_4Cl	2	3	0	0
Al^0	26	20	34	27

Table 11: quantitative analysis of sample B extinguished surface

Id.	Grazing incidence		Bragg-Brentano	
	Mass %	Volume %	Mass %	Volume %
NH_4ClO_4	58	65	62	69
α-NH_4Cl	1	2	0	0
Al^0	41	33	38	31

7. Conclusion

The paper presented a set of analyses which scrutinized the properties of two nominally identical hematite batches, beyond the typical approach used in industrial quality assurance processes. SEM and laser granulometry featured quite homogeneous results but a detailed investigation showed different properties which are clues of material variability. For example, the ICP pointed out the existence of chemical contamination by other metals and of sulfur, probably connected to the production process. The XRD highlighted the possible presence of different iron oxides (e.g. magnetite). Despite such differences, the thermal and the combustion behaviors of propellants containing the additives were overlapped and included within the band of variability. In some cases, the error bars were widened by deficiency in material dispersion, showing indirectly different attitude to uniformly spread in media. In this respect, cohesive clustering appears to be a very important parameter for the application of a propellant catalyst and deserves a specific consideration and further analysis. Comparison with baseline compositions demonstrate a homogeneous effectiveness of the two batches as ballistic modifier at the tested concentration.

The importance in quality control and monitoring of powders becomes of paramount importance when the repeatability of performance is foreseen. The reader should be warned that not all the differences may cause a visible modification in the final catalyst attitude, even though a clear view can be gained after a specific experimental campaign. In this respect, a standard characterization approach can be sufficient to grant a continuative monitoring over a production process but a wider and customized protocol has to be implemented if a detailed fingerprint of a powder is needed.

Acknowledgements

The activity has been financed by ESA in the frame of the Ariane exploitation accompaniment programme (ARTA in the past, LEAP currently)

References

1. J.P. Sutton and O. Biblarz, Rocket Propulsion Elements, Seventh Edition, John Wiley & Sons, New York, 2001.

2. S. Chakravarty, E.W. Price, R.K. Sigman, Mechanism of Burning Rate Enhancement of Composite Solid Propellants by Ferric Oxide, J. Propul. Power 13 (1997) 471-480.

3. K. Kishore, V.R.P. Verneker and M.R. Sunitha, Effect of Catalyst Concentration on Burning Rate of Composite Solid Propellants, AIAA J., 15 (1977) 1649-1651

4. R.M. Cornell and U. Schwertmann, The Iron Oxides, Second Edition, Wiley-VCH, Weinheim, 2003

5. T. Danno, D. Nakatsuka, Y. Kusano, H. Asaoka, M. Nakanishi, T. Fujii, Y. Ikeda, and J. Takada, Crystal Structure of β Fe2O3 and Topotactic Phase Transformation to α Fe2O3, Cryst. Growth Des. 13 (2013) 770−774

6. R. Zboril, M. Mashlan, and D. Petridis, Iron(III) Oxides from Thermal Processes-Synthesis, Structural and Magnetic Properties, Mossbauer Spectroscopy Characterization, and Applications, Chem. Mater. 14 (2002) 969-982

7. Anon. Maghemite. In: Handbook of Mineralogy, J.W. Anthony, R.A. Bideaux, K.W. Bladh, and M.C. Nichols, Eds., Mineralogical Society of America, Chantilly, VA 20151-1110, USA. http://www.handbookofmineralogy.org/ (accessed on 27/05/2018)

8. S. Kachi, K. Momiyama, and S. Shimizu, An Electron Diffraction Study and a Theory of the Transformation from γ-Fe2O3 to α-Fe2O3, J. Ph. Soc. Jpn., 18 (1963) 106-116

9. S. I. Srikrishna Ramya and C. K. Mahadevan, Effect of calcination on the electrical properties and quantum confinement of Fe2O3 nanoparticles, IMPACT:IJRET, 3 (2014) 570-581

10. R. Zboril, M. Mashlan, and D. Petridis, Iron(III) Oxides from Thermal Processes-Synthesis, Structural and Magnetic Properties, Mossbauer Spectroscopy Characterization, and Applications, Chem. Mater. 14 (2002) 969-982

11. K. Kelm and W. Mader, Synthesis and Structural Analysis of ε-Fe2O3, Z. Anorg. Allg. Chem. 631 (2005) 2383-2389

12. J. Tuček, L. Machala, S. Ono, A. Namai, M. Yoshikiyo, K. Imoto, H. Tokoro, S. Ohkoshi, and R. Zbořil, Zeta-Fe2O3 – A new stable polymorph in iron (III) oxide family, Sci. Rep., 5 (2015) 15091.

13. L. Blaney, Magnetite (Fe3O4): Properties, Synthesis, and Applications, Leigh Review, Vol. 15, Paper 5, Leigh University, 2007

14. Z. Ma, F. Li, and H. Bai, Effect of Fe2O3 in Fe2O3/AP Composite Particles on Thermal Decomposition of AP on Burning Rate of the Composite Propellant, Propell. Explos. Pyrot., 31 (2006) 447-451

15. S.S. Joshi, P.R. Patil, and V.N. Krishnamurthy, Thermal Decomposition of Ammonium Perchlorate in the Presence of Nanosized Ferric Oxide, Def. Sci. J., 58 (2008) 721-727

16. W. Wang and J. Yao, Catalytic Activity of Magnetite with Different Shapes for the Thermal Decomposition of Ammonium Perchlorate, Chem. Lett., 43 (2014) 1554:1556

17. Y. Oyumi, T. Anan, H. Bazaki, and T. Harada, Plateau Burning Characteristics of AP Based Azide Composite Propellants, Propell. Explos. Pyrot. 20 (1995) 150-155.

18. P.R. Patil,V.N. Krishnamurthy, and S.S. Joshi, Differential Scanning Calorimetry Study of HTPB based Composite Propellants in Presence of Nano Ferric Oxide, Propell. Explos. Pyrot., 31 (2006) 442-446.

19. R.A. Frederick Jr., J.J. Whitehead; L.R. Knox; and M.D. Moser, Regression Rates Study of Mixed Hybrid Propellants, J. Propul. Power, 23 (2013) 175-180.

20. X. Liu, J. Hao, and S. Gaan, Recent Studies of Decomposition and Strategies of Smoke and Toxicity Suppression for Polyurethane-based Materials. RSC Adv, 6 (2016) 74742-74756

21. L. Durães, B.F.O. Costa, R. Santos, A. Correia, J. Campos, and A. Portugal, Fe2O3/Aluminum Thermite Reaction Intermediate and Final Products Characterization, Mat. Sci. Eng. A-Struct. 465 (2007) 199–210.

22. V.P. Zhdanov, Impact of Surface science on the Understanding of Kinetics of Heterogeneous Catalytic Reactions, Surf. Sci., 500 (2002) 966-985.

23. J.H. Sinfelt, Role of Surface Science in Catalysis, Surf. Sci., 500 (2002) 923-946.

24. AA.VV. Chemical composition, In: Springer Book of Materials Measurement Methods. Chapter 4. Eds: H. Czichos T. Saito, and L. Smith, Springer Science and Business Media, Springer-Verlag, Berlin, Heidelberg, 2006

25. R.W. Cheary, A.A. Coelho, A Fundamental Parameter Approach of X-ray Line-profile Fitting, J. Appl. Crystallogr. 25 (1992) 109–121

26. H.M. Rietveld, A Profile Refinement Method for Nuclear and Magnetic Structures, J. Appl. Cryst. 2 (1969) 65-71

27. T.L. Boggs, D.E. Zurn, H.F. Cordes, and J. Covino, Combustion of Ammonium Perchlorate and Various Inorganic Additives, J. Propulsion, 4 (1988) 27-39

28. A. Ishihara and M.Q. Brewster, Combustion Studies of Boron, Magnesium, and Aluminum Composite Propellants, Combustion Science and Technology, 87 (1993) 275-290

29. S. Brunauer, P.H. Emmett, and E. Teller,Adsorption of Gases in Multimolecular Layers, J. Am. Chem. Soc., 60 (1938) 309–319

30. Resodyn LabRAM, http://resodynmixers.com/products/labram/ (accessed 06 Dec 16).

31. W.W. Wendlandt, Thermal Analysis, Third Edition, John Wiley & Sons, New York, 1986.

32. A. V. Raevskii, G. B. Manelis, V. V. Boldyrev, L. A. Votinova, The Role of Dislocations in the Thermal Decomposition of Ammonium Perchlorate Crystals, Dokl. Akad. Nauk SSSR, 160 (1965) 1136–1137 (in Russian language)

33. G.B. Manelis and Ju. I. Rubtsov, Kinetics of the Thermal Decomposition of Ammonium Perchlorate, Zhurnal Fisicheskoi Khimii, 40 (1966) 770-774 (translation from Russian language, DTIC Accession Number AD0651748)

34. W.A.Rosser, S.H.Inami and H.Wise, Thermal Decomposition of Ammonium Perchlorate, Combust. Flame, 12 (1968) 427-435.

35. Y-C Lu and K.K.Kuo, Thermal Decomposition Study of Hydroxyl-terminated Polybutadiene (HTPB) Solid Fuel, Thermochim. Acta, 275 (1996) 181-191

36. J.A.F.F. Rocco, J.E.S. Lima, A.G. Frutuoso, K.Iha, M. Ionashiro, J.R. Matos, M.E.V. Suárez-Iha, Thermal degradation of a composite solid propellant examined by DSC, J. Therm. Anal. Calorim. 75 (2004) 551–557.

37. C. Zanotti, A. Volpi, M. Bianchessi, and L.T. DeLuca, Measuring Thermodynamic Properties of Burning Propellants, In: Nonsteady Burning and Combustion Stability of Solid Propellants, L.T. De Luca and E.W. Price and M. Summerfield (eds.), Progress in Astronautics and Aeronautics Series, Vol. 143, AIAA, Washington, DC, USA, pp. 145-196, 1990.

38. L.T. DeLuca, F. Maggi, S. Dossi, M. Fassina, C. Paravan, and A. Sossi, Prospects of Aluminum Modifications as Energetic Fuels in Chemical Rocket Propulsion, In: Chemical Rocket Propulsion, Springer Nature, pp. 191-233, 2016.

39. V.V. Boldyrev, Thermal Decomposition of Ammonium Perchlorate, Thermochim Acta 443 (2003) 1-36

40. A.G. Keenan and R.F. Siegmund, Thermal Decomposition of Ammonium Perchlorate, Q. Rev. Chem. Soc., 23 (1969) 430-452

41. A. Bandera, F. Maggi, and L.T. DeLuca, Agglomeration of Aluminized Solid Rocket Propellants, AIAA Paper No. 2009-5439, 2009

42. C. Bruno, G. Riva, C. Zanotti, R. Dondè, C. Grimaldi, and L.T. DeLuca, Experimental and Theoretical Burning of Solid Rocket Propellants Near the Pressure Deflagration Limit, Acta Astronaut., 12 (1985) 351-360